Materials Research. 2026; 29(suppl. 2): e20260161
DOI: https://doi.org/10.1590/1980-5373-MR-2026-0161

Phase-Proportion-Dependent Structural Stability in c-BN/h-BN Heterostructures

Pedro Altero Parra*[a], *Xiang Zhang*[b], *Pulickel M. Ajayan*[b], *Eliezer F. Oliveira*[c]

[a]*Universidade Estadual Paulista (UNESP), Faculdade de Ciências, Programa de Pós-Graduação em Ciência e Tecnologia de Materiais (POSMAT), Bauru, SP, Brasil.*
[b]*Rice University, Department of Materials Science and Nanoengineering, Houston, TX, United States.*
[c]*Universidade Estadual Paulista (UNESP), Faculdade de Ciências, Departamento de Física e Meteorologia, Bauru, SP, Brasil.*

Received: May 12, 2026; Revised: July 13, 2026; Accepted: July 25, 2026

In this work, Density Functional Theory (DFT) calculations were employed to investigate the structural stability and magnetic behavior of c-BN/h-BN heterostructures with different phase proportions (20/80, 40/60, 50/50, 60/40, and 80/20). The results reveal that heterostructures containing thin c-BN regions (20/80 and 40/60) undergo pronounced structural reconstruction toward hexagonal-like configurations during relaxation. In contrast, higher c-BN concentrations (50/50, 60/40, and 80/20) preserve the coexistence of sp^2- and sp^3-like arrangements, exhibiting enhanced structural stability and reduced interfacial distortions. Additionally, localized magnetic ordering emerges only in the heterostructures that preserve the cubic domains, indicating a strong correlation between the magnetic response and the stability of the sp^3 network. These findings demonstrate that the structural and magnetic properties of c-BN/h-BN heterostructures are strongly governed by the cubic phase proportion.

Keywords*: Density Functional Theory, c-BN/h-BN Heterostructures, Structural Stability.*

1. Introduction

Boron nitride (BN) is a material of considerable scientific and technological interest due to the wide variety of physical properties exhibited by its allotropes, analogous to carbon-based materials such as graphite and diamond[1]. Among its phases, cubic boron nitride (c-BN), characterized by sp^3 hybridization, and hexagonal boron nitride (h-BN), with sp^2 hybridization, are the most extensively studied[2]. c-BN exhibits exceptional hardness, high thermal conductivity, and a wide band gap, making it a promising material for high-power microelectronics and protective coatings[3]. In contrast, h-BN, often referred to as "white graphene", is a chemically inert wide-band-gap insulator widely employed in two-dimensional applications and dielectric devices[4].

Recently, significant attention has been devoted to combining these two phases into nanostructured heterostructures in order to achieve materials with tunable structural and electronic properties[5]. Theoretical studies have suggested that the c-BN/h-BN interface can promote band-gap modulation and induce new interfacial electronic states[6]. However, previous investigations have mainly focused on heterostructures containing approximately equal proportions of c-BN and h-BN (50/50 ratio)[7,8].

Despite these advances, a systematic understanding of how the structural stability of c-BN/h-BN heterostructures evolves as a function of phase proportion remains lacking[9]. In particular, it is still unclear whether the cubic phase can preserve its sp^3-bonded network when confined to ultrathin regions surrounded by h-BN domains.

In this context, we perform a first-principles study based on Density Functional Theory (DFT) calculations to investigate the structural stability and magnetic behavior of c-BN/h-BN heterostructures with different phase proportions (20/80, 40/60, 50/50, 60/40, and 80/20). Special attention is devoted to understanding the influence of the cubic phase thickness on structural reconstruction, interfacial stability, and localized magnetic ordering.

2. Materials and Methods

To investigate the structural stability of the c-BN/h-BN heterostructures, first-principles calculations based on DFT[10] and the Projector Augmented Wave (PAW) method[11] were employed. Since the proposed heterostructures contain h-BN regions, whose interlayer interactions are predominantly governed by van der Waals forces, dispersion effects were included using the Grimme D3 correction[12]. The self-consistent calculations were considered converged when the total energy variation was lower than 10^{-6} Ry, while structural optimization was terminated when the residual forces acting on all atoms were smaller than 10^{-3} Ry/Bohr. All calculations were carried out using the Quantum ESPRESSO package[13] within the PBE exchange-correlation functional[14] and including spin polarization. Structural modeling and visualization were performed using VMD[15] and Avogadro[16]. Prior to the production calculations, systematic convergence tests were performed for both the plane-wave cutoff energy and the Monkhorst-Pack k-point sampling. The total energy variation was monitored as a function of these parameters until numerical convergence was achieved.

*e-mail: eliezer.oliveira@unesp.br
Associate Editor: Luis Cabral.
Editor-in-Chief: Luiz Antonio Pessan.

Based on these tests, a cutoff energy of 80 Ry and a 6 x 6 x 1 Monkhorst-Pack grid were selected because further increases produced negligible variations in the total energy while considerably increasing the computational cost. The corresponding convergence curves are presented in Figure 1.

The heterostructures were constructed from unit cells obtained from the Materials Project database[17]. The initial c-BN structure was oriented along the [111] crystallographic direction and contained 24 atoms, while the h-BN structure was oriented along the [0001] direction with 16 atoms, following orientations commonly observed in experimental synthesis[18]. The c-BN and h-BN unit cells were replicated according to a 2 x 2 x 4 and 2 x 2 x 6, respectively, resulting in both structures containing 96 atoms (48 boron and 48 nitrogen atoms). After structural relaxation, the optimized lattice parameters are summarized in Table 1.

As shown in Table 1, the optimized lattice parameters a and b converge to 5.026 Å and 5.132 Å for the h-BN and c-BN structures, respectively. For h-BN, the obtained value is in excellent agreement with the experimental lattice constant of 2.50 Å[19], corresponding to 5.00 Å in the 2 × 2 expanded basal-plane supercell. For the c-BN phase, the optimized lattice parameter of 5.132 Å is also consistent with the experimental cubic lattice constant of 3.61 Å[20,21].

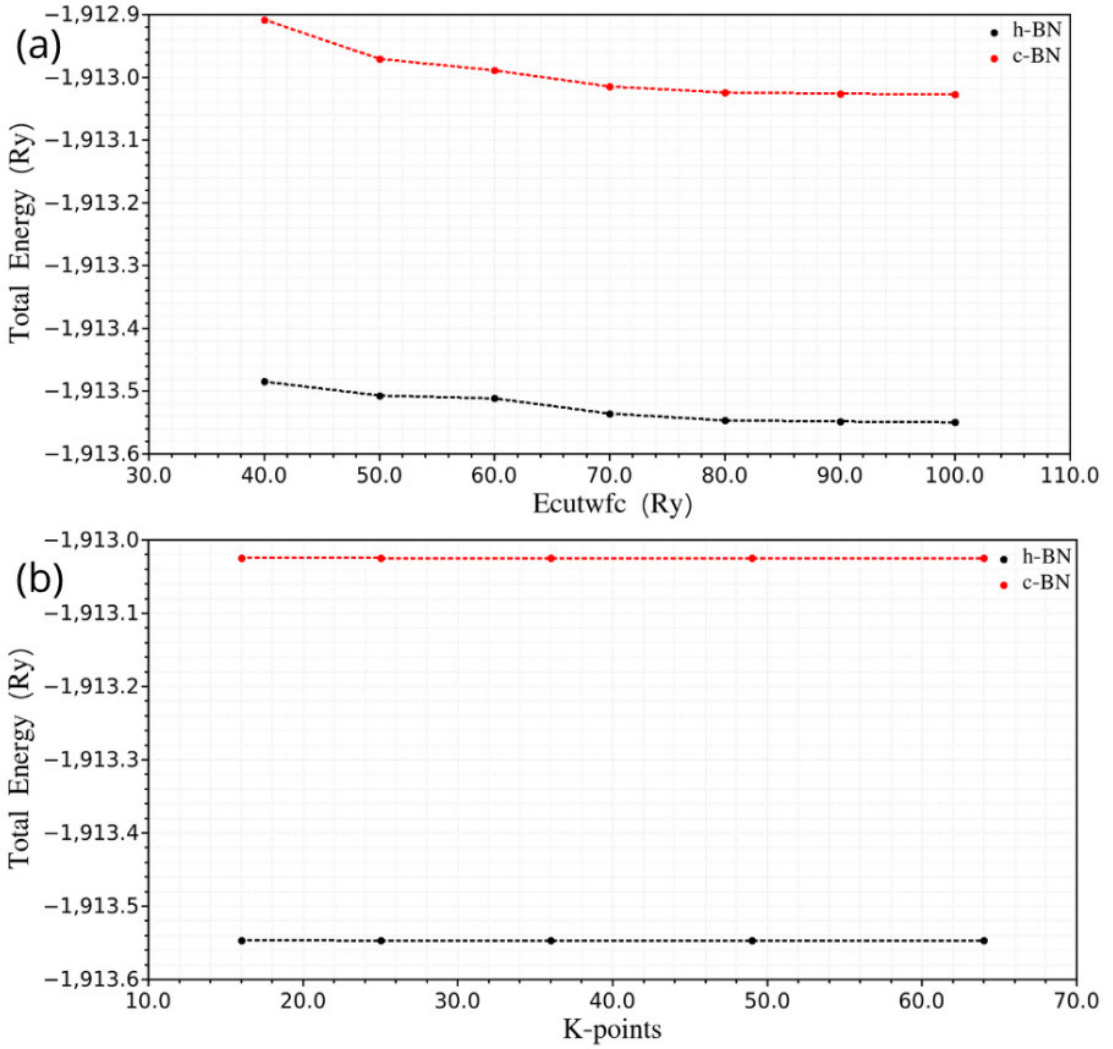

Figure 1. Convergence of the total energy for bulk c-BN and h-BN with respect to (a) the plane-wave kinetic energy cutoff and (b) the total number of k-points in the Monkhorst–Pack sampling (N_x x N_y x N_z).

Table 1. Lattice parameters of pure c-BN and h-BN structures before and after structural relaxation.

Parameter	c-BN (Before)	c-BN (After)	h-BN (Before)	h-BN (After)
a (Å)	5.128	5.132	5.025	5.026
b (Å)	5.128	5.132	5.025	5.026
c (Å)	25.120	25.142	46.242	41.074

Considering the [111] surface orientation adopted in this work, the corresponding in-plane lattice periodicity is given by $a_{(111)}=a_{cubic}/\sqrt{2}$, resulting in a reference value of approximately 5.105 Å. The small deviations obtained for both phases (less than 0.6%) indicate that the computational approach and the dispersion corrections employed provide an accurate description of the structural properties of these systems.

Regarding the lattice parameter along the c direction, the optimized h-BN structure exhibits a contraction from 46.242 Å to 41.074 Å, corresponding to an overall reduction of approximately 11.2%. This contraction reflects the relaxation of the interlayer spacing toward the equilibrium distance predicted by the PBE exchange-correlation functional including the Grimme D3 dispersion correction. Initially, the h-BN model was constructed using crystallographic lattice parameters, whereas structural optimization allows the adjacent BN layers to approach each other until the attractive van der Waals interactions are balanced by the short-range Pauli repulsion. Consequently, the average interlayer spacing decreases from approximately 3.85 Å to 3.42 Å, in good agreement with previous theoretical studies employing dispersion-corrected DFT methods[17,19,20]. In contrast, the in-plane B–N bond lengths remain close to their equilibrium values, approximately 1.45 Å for h-BN and 1.57 Å for c-BN, confirming that the structural relaxation primarily affects the weak interlayer interactions rather than the strong covalent bonds within each layer[17,19,20].

After obtaining the optimized structures of pure h-BN and c-BN, the c-BN/h-BN heterostructures were constructed with phase proportions of 20/80, 40/60, 50/50, 60/40, and 80/20. To construct coherent c-BN/h-BN heterostructures, the in-plane lattice parameters were fixed to those of the fully optimized c-BN structure (a = b = 5.132 Å), while the out-of-plane lattice parameter (c) was adjusted according to the relative thickness of each phase. This strategy was adopted because cubic BN is considerably stiffer than hexagonal BN, exhibiting a significantly higher elastic modulus. Therefore, c-BN was used as the structural reference, whereas the mechanically more compliant h-BN layers were allowed to elastically accommodate the in-plane strain required to form a coherent interface. Such an approach is physically justified and has been widely employed in first-principles studies of lattice-mismatched heterostructures, where the softer constituent preferentially accommodates the elastic deformation. The in-plane lattice mismatch between the isolated optimized phases was evaluated as $f = (a_{h\text{-}BN} - a_{c\text{-}BN})/a_{c\text{-}BN}$, where $a_{h\text{-}BN}$ and $a_{c\text{-}BN}$ are the equilibrium lattice parameters of hexagonal and cubic BN, respectively. Using the optimized lattice constants, a mismatch of approximately −2.06% was obtained. Consequently, after constructing the heterostructures, the h-BN layers accommodate an approximately 2.06% tensile in-plane strain relative to their equilibrium lattice parameter, while the c-BN lattice remains essentially unstrained. Since the same in-plane lattice parameters were adopted for all models, this mismatch remains the same for the 20/80, 40/60, 50/50, 60/40, and 80/20 phase proportions.

The phase proportions were defined based on the relative atomic percentage of the c-BN and h-BN regions within the heterostructure. The initial interfacial distance between the c-BN and h-BN layers was set to 3.0 Å, and periodic boundary conditions were applied in all directions. The initial c lattice parameters adopted for each configuration are summarized in Table 2.

The heterostructures were structurally relaxed by allowing the atomic positions and the c lattice parameter to vary, while the in-plane lattice parameters remained fixed. Spin-polarized calculations were performed by assigning an initial magnetic moment to the c-BN regions in order to investigate the possible emergence of localized spin polarization associated with interfacial reconstruction and undercoordinated surface atoms.

3. Results and Discussion

Figure 2 presents the initial and optimized atomic configurations of the c-BN/h-BN heterostructures with phase proportions of 20/80 and 40/60. In both cases, structural relaxation induces significant atomic rearrangements, particularly within the regions initially assigned to the cubic phase, indicating that ultrathin c-BN domains become structurally unstable when embedded in a predominantly hexagonal matrix. For the 20/80 heterostructure (Figure 2a), the initial thicknesses of the c-BN and h-BN regions were approximately 2.6 Å and 30.8 Å, respectively. After structural optimization, the region initially associated with the cubic phase expands to approximately 3.4 Å, while the h-BN region increases slightly to 31.1 Å, corresponding to thickness variations of +28.6% and +0.8%, respectively. The optimized structure reveals a pronounced loss of the original tetrahedral coordination, with the atoms reorganizing into configurations that closely resemble the hexagonal phase.

A similar behavior is observed for the 40/60 heterostructure (Figure 2b). The thickness of the c-BN region increases from approximately 6.8 Å to 10.3 Å (+51.6%), whereas the h-BN region exhibits only a marginal increase, from 23.9 Å to 24.0 Å (+0.2%). The much larger structural rearrangement occurring within the cubic region indicates that ultrathin c-BN domains cannot fully preserve their tetrahedral sp^3 network under ambient-pressure conditions. Instead, the system lowers its total energy through local bond reconstruction toward hexagonal-like configurations, while the h-BN domains remain essentially unchanged due to their higher thermodynamic stability[20,22].

The structural reconstruction observed in the ultrathin c-BN domains originates from the competition among bulk stability, surface energy, and interfacial energy. Although cubic BN is a metastable phase that can persist under ambient conditions because of the large kinetic barrier separating it from h-BN[23], this stability progressively decreases as the thickness of the cubic region is reduced. At the nanoscale, the increasing surface-to-volume ratio enhances the contribution of surface and interface energies to the total energy of the system[24].

Table 2. Initial c lattice parameters of the c-BN/h-BN heterostructures before structural relaxation.

Parameter/Proportion	20/80	40/60	50/50	60/40	80/20
c (Å)	39.455	36.795	34.131	31.471	28.807

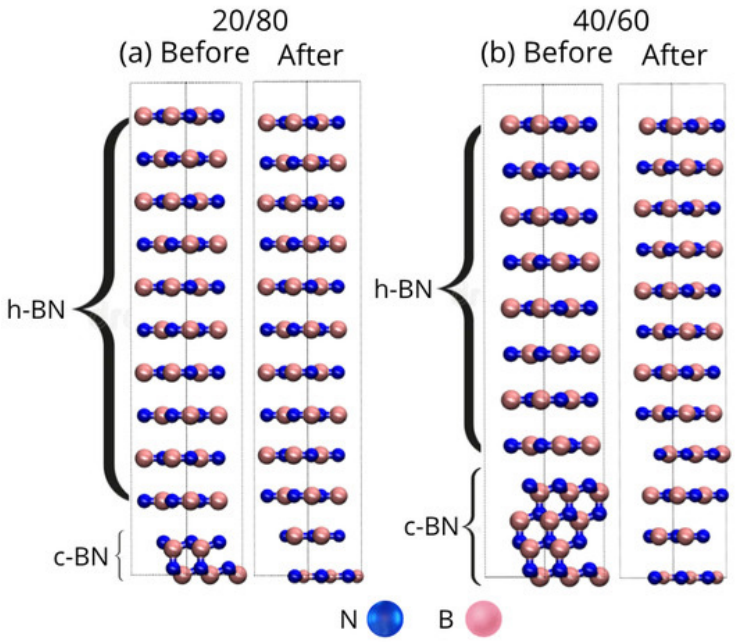

Figure 2. Atomic configurations of the (a) 20/80 and (b) 40/60 c-BN/h-BN heterostructure before and after geometry optimization.

Consequently, the energetic cost of preserving the tetrahedrally coordinated sp^3 network becomes comparable to, or even greater than, the energy required for local bond reconstruction. Furthermore, the surrounding h-BN layers provide a crystallographic template that naturally favors trigonal sp^2 coordination, facilitating local atomic rearrangements near the interface. As a result, the system minimizes its total energy through partial reconstruction of the ultrathin cubic domains into hexagonal-like configurations. This behavior should therefore be interpreted as an interface-driven structural reconstruction resulting from finite-size effects and energetic competition between the two BN polymorphs, rather than as a pressure-induced bulk c-BN→h-BN phase transition. Conversely, the h-BN layers remain essentially unchanged because h-BN is the thermodynamically stable BN phase under ambient-pressure conditions and already possesses the lowest-energy sp^2 bonding configuration, leaving no driving force for the reverse transformation during structural relaxation. This interpretation is consistent with the structural evolution observed in Figure 2, where the heterostructures containing the thinnest c-BN regions (20/80 and 40/60) exhibit the most pronounced atomic reconstruction, whereas heterostructures with thicker c-BN domains preserve most of the tetrahedrally coordinated cubic framework and remain structurally stable after relaxation.

The atomic rearrangement from the initial cubic configuration toward hexagonal-like arrangements can be quantitatively analyzed through the Radial Distribution Function, g(r), shown in Figure 3. The figure presents the individual g(r) profiles of the c-BN and h-BN regions for the 20/80 and 40/60 heterostructures before and after structural optimization. For the c-BN regions in both heterostructures (Figures 3(a) and 3(c)), a pronounced shift is observed in the first coordination shell. Before relaxation (black curves), the primary peak is centered at approximately 1.57 Å, corresponding to the characteristic B–N bond length of the cubic diamond-like structure. After relaxation (red curves), this peak shifts to approximately 1.48 Å, which is consistent with the equilibrium bond length of the h-BN phase. The reduction in bond length from 1.57 Å to 1.48 Å for the 20/80 and 40/60 heterostructures is associated with the structural reorganization of the original sp^3-bonded cubic network into more stable sp^2-like configurations. Simultaneously, the increase in the thickness of the c-BN regions after relaxation suggests a progressive loss of the compact tetrahedral arrangement characteristic of the cubic phase.

In contrast, the g(r) profiles associated with the h-BN regions (Figures 3(b) and 3(d)) remain nearly unchanged throughout the relaxation process, indicating the structural stability of the hexagonal phase. Additionally, the similarity between the long-range coordination profiles of both phases after relaxation, particularly beyond 3.0 Å, suggests a substantial loss of the initial cubic ordering and the emergence of a predominantly hexagonal-like structural arrangement. Collectively, these results reinforce the tendency of thin c-BN regions to reconstruct into energetically more favorable hexagonal-like configurations in the presence of dominant h-BN domains.

To investigate whether the tendency of thin c-BN regions to reconstruct into hexagonal-like configurations is intrinsically related to the cubic phase or influenced by the presence of h-BN domains, additional simulations were performed for isolated c-BN slabs, as shown in Figure 4. The optimized atomic configurations provide clear evidence of a critical thickness required to preserve the sp^3 hybridization characteristic of the cubic phase. For the 2-layer c-BN slab (Figures 4(a) and 4(b)), corresponding to the c-BN thickness observed in the 20/80 heterostructure, a complete structural reconstruction is observed after relaxation.

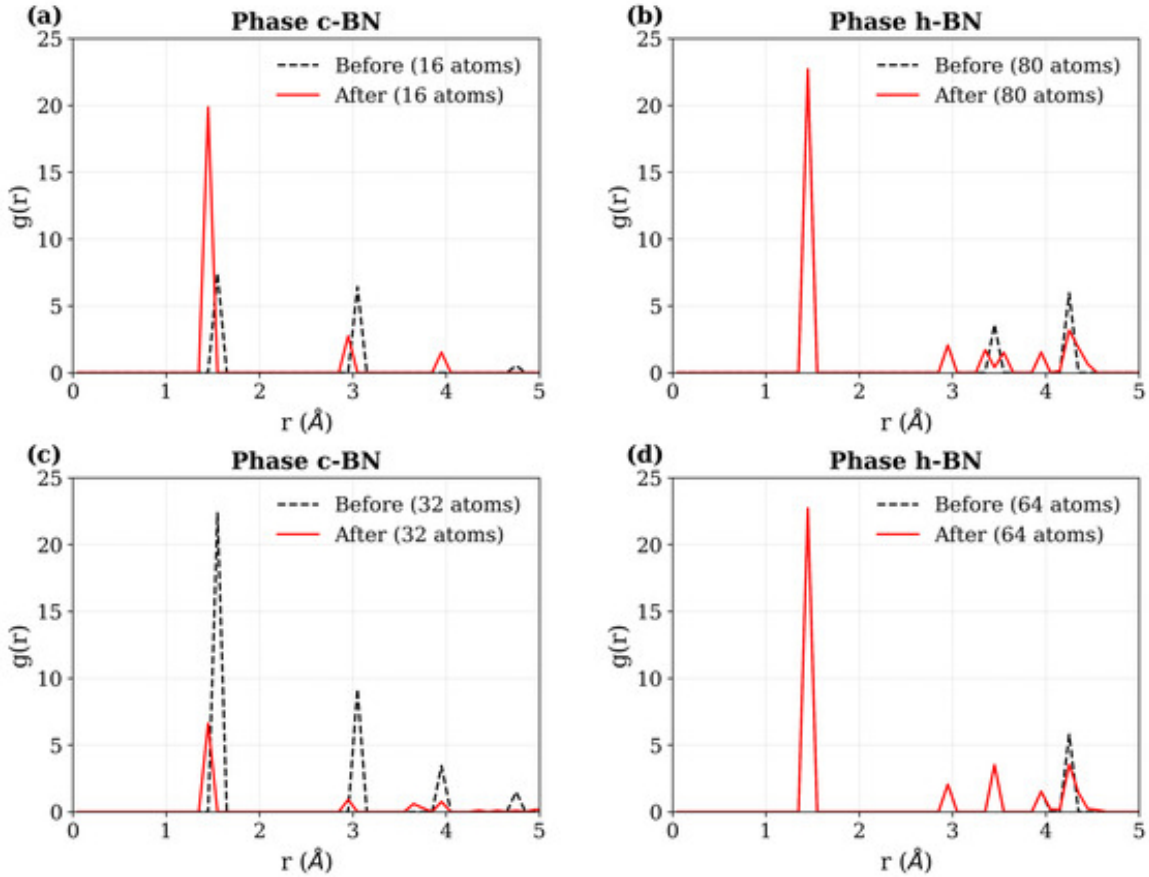

Figure 3. Radial Distribution Function, g(r), of the c-BN and h-BN regions for the 20/80 and 40/60 c-BN/h-BN heterostructures before and after structural relaxation: (a) c-BN and (b) h-BN regions for the 20/80 heterostructure, (c) c-BN and (d) h-BN regions for the 40/60 heterostructure. Black dashed lines correspond to the as-built structures, while red solid lines represent the optimized configurations.

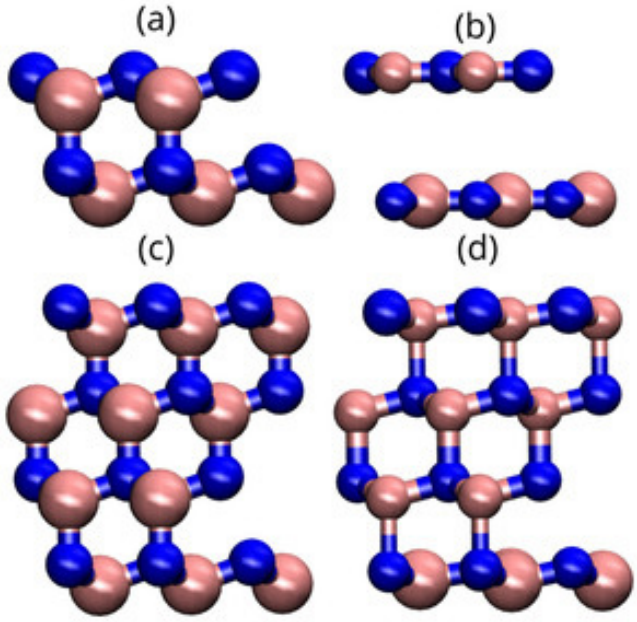

Figure 4. Atomic configurations of isolated c-BN slabs before and after structural relaxation: (a) initial and (b) optimized 2-layer c-BN slab, (c) initial and (d) optimized 4-layer c-BN slab.

In this case, the original tetrahedral network collapses into two decoupled hexagonal-like layers. In contrast, the 4-layer c-BN slab (Figures 4(c) and 4(d)), representative of the c-BN thickness in the 40/60 heterostructure, undergoes only partial reconstruction. While the surface layers become more planar, with bond distances decreasing from 1.57 Å to 1.49 Å, the inner layers preserve part of their original cubic coordination. This behavior suggests that the surface regions tend to reorganize toward more energetically favorable hexagonal-like configurations, while the inner layers retain sufficient stability to partially preserve the cubic network.

This behavior becomes particularly relevant when compared to the 40/60 heterostructure, where the c-BN regions exhibited a much more pronounced loss of cubic ordering. The comparison suggests that the h-BN domains actively contribute to the structural transformation of the cubic phase. Although the isolated 4-layer slab retains sufficient intrinsic stability to partially preserve its sp^3 network, the interaction with the h-BN regions within the heterostructure appears to facilitate the structural reorganization toward hexagonal-like arrangements by lowering the energetic cost associated with the reorganization of the remaining sp^3 bonds.

The structural evolution of the c-BN/h-BN heterostructures with higher concentrations of the cubic phase (50/50, 60/40, and 80/20) reveals a different behavior compared to the lower concentration models discussed previously. As shown in Figure 5, structural relaxation no longer induces a complete loss of cubic ordering. Instead, both cubic (sp^3-like) and hexagonal (sp^2-like) arrangements remain preserved after optimization.

For the 50/50 heterostructure, the interfacial distance between the c-BN and h-BN regions is 3.14 Å upon relaxation. Additionally, the distance between adjacent h-BN layers is approximately 3.45 Å. Furthermore, a clear separation between the c-BN and h-BN regions is preserved after structural relaxation, as shown in Figure 5(a). Although local distortions are observed near the interface, the cubic region maintains most of its original tetrahedral coordination, indicating enhanced structural stability compared to the 20/80 and 40/60 heterostructures. This behavior is further supported by the Radial Distribution Function g(r) analysis shown in Figures 6(a) and 6(b). The figure presents the individual g(r) profiles calculated separately for the c-BN (Figure 6(a)) and h-BN (Figure 6(b)) regions of the heterostructures before and after structural relaxation. For the c-BN region (Figure 6(a)), the primary peak remains centered near the characteristic sp^3 B–N bond distance, exhibiting only a slight shift and broadening after relaxation. The bond length decreases from 1.58 Å (before relaxation, black curve) to 1.56 Å (after relaxation, red curve), indicating a relatively small structural rearrangement when compared to the lower c-BN concentration heterostructures. In contrast, no significant changes are observed for the h-BN region (Figure 6(b)), with the characteristic bond length remaining approximately at 1.48 Å throughout the relaxation process. Simultaneously, only minor variations in the thicknesses of the c-BN (11.0 Å to 10.9 Å, -0.9%) and h-BN (17.1 Å to 17.3 Å, +1.2%) regions are observed after relaxation, suggesting that both phases preserve their structural identities. These results indicate that, at the 50/50 proportion, the c-BN network possesses sufficient intrinsic stability to maintain its sp^3-like arrangement, while the h-BN regions accommodate most of the interfacial strain.

For the 60/40 heterostructure, the optimized interfacial distance between the c-BN and h-BN regions is approximately 3.35 Å, while the spacing between adjacent h-BN layers remains close to 3.44 Å. The higher concentration of the cubic phase further stabilizes the sp^3 network, leading to even smaller structural variations after relaxation.

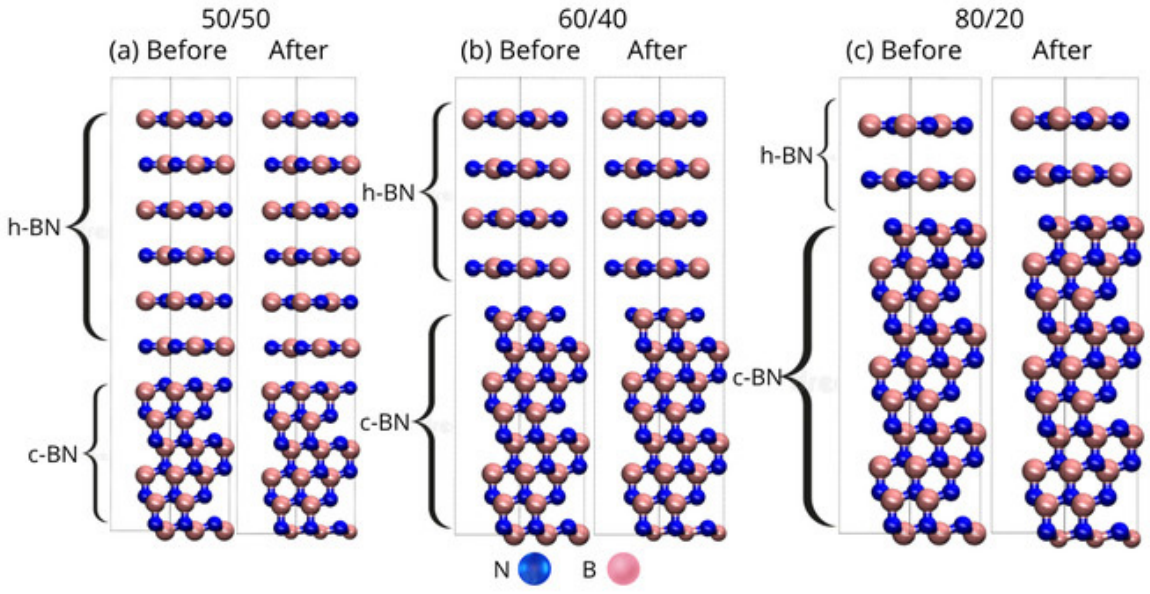

Figure 5. Atomic configurations of the (a)50/50, (b) 60/40, and (c) 80/20 c-BN/h-BN heterostructure before and after geometry optimization.

The atomic configurations shown in Figure 5(b) reveal a well-preserved interface, where both the cubic and hexagonal regions maintain their structural identities with only minor interfacial distortions. This behavior is corroborated by the Radial Distribution Function g(r) analysis presented in Figures 6(c) and 6(d), where the g(r) profiles were calculated separately for the c-BN and h-BN regions of the heterostructure. For the c-BN region (Figure 6(c)), the primary peak remains highly intense and sharply defined after relaxation, indicating the preservation of long-range crystalline order within the cubic phase. The characteristic B–N bond length exhibits only a minimal variation, decreasing from 1.58 Å before relaxation (black curve) to 1.57 Å after relaxation (red curve). Similarly, the h-BN region (Figure 6(d)) remains structurally stable, preserving its characteristic bond length near 1.48 Å. In addition, only minor thickness variations are observed for both phases after relaxation, with the c-BN region decreasing from 15.2 Å to 15.0 Å (-1.3%), while the h-BN region maintains a thickness of 10.3 Å before and after relaxation. This indicates that the interfacial strain is insufficient to induce significant structural reconstruction. These results suggest that the 60/40 proportion corresponds to a structurally stable regime in which both sp^2- and sp^3-like configurations coexist within the same heterostructure while preserving their respective structural characteristics.

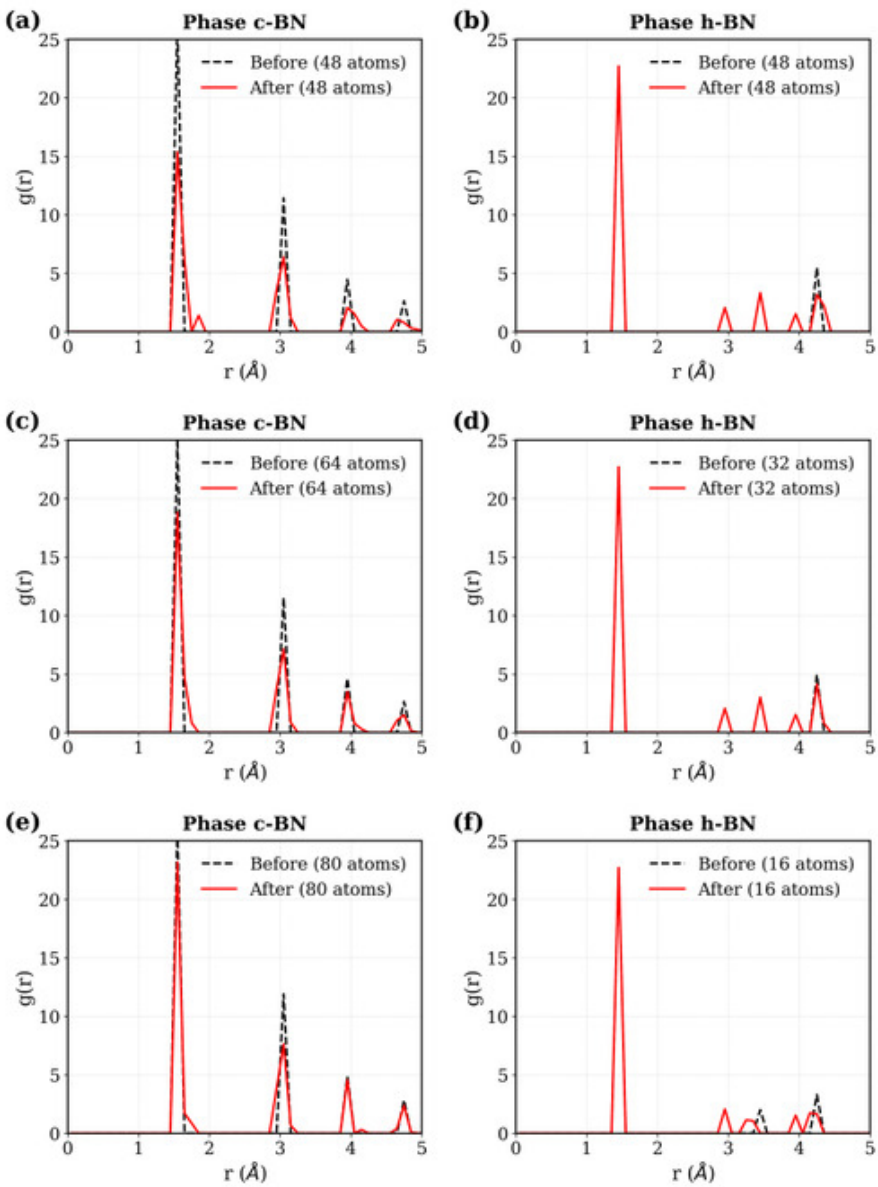

Figure 6. Radial Distribution Function, g(r), of the c-BN and h-BN regions for the 50/50, 60/40, and 80/20 c-BN/h-BN heterostructures before and after structural relaxation: (a) c-BN and (b) h-BN regions for the 50/50 heterostructure, (c) c-BN and (d) h-BN regions for the 60/40 heterostructure, (e) c-BN and (f) h-BN regions for the 80/20 heterostructure. Black dashed lines correspond to the as-built structures, while red solid lines represent the optimized configurations.

Table 3. Summary of the magnetic signatures observed for the c-BN/h-BN heterostructures after structural relaxation.

Proportion	Total Magnetization (μB/atom)	Absolute Magnetization (μB/atom)	Magnetic Signature
20/80	0.000	0.000	Magnetic quenching
40/60	0.000	0.000	Magnetic quenching
50/50	-0.040	0.049	Localized spin polarization
60/40	0.000	0.060	Antiferromagnetic-like compensation
80/20	-0.029	0.032	Localized spin polarization

For the 80/20 heterostructure, where the cubic phase becomes largely predominant, the system exhibits structural behavior closely resembling that of a highly stable c-BN network containing thin hexagonal regions. Upon relaxation, the interfacial distance is 3.13 Å, while the spacing between adjacent h-BN layers remains approximately 3.36 Å. The optimized atomic configuration shown in Figure 5(c) presents only minor deviations relative to the initial structure, confirming the high structural stability of the sp^3 framework. This behavior is further supported by the Radial Distribution Function g(r) analysis presented in Figures 6(e) and 6(f), where the g(r) profiles were calculated separately for the c-BN and h-BN regions of the heterostructure. For both phases, the g(r) profiles before and after relaxation remain highly similar, particularly within the first coordination shell, indicating minimal structural rearrangement during optimization. For the c-BN region (Figure 6(e)), the characteristic B–N bond length of 1.58 Å remains essentially unchanged after relaxation, while only minor thickness variations are observed (from 19.4 Å to 19.3 Å, corresponding to a variation of -0.5%). In contrast, the h-BN region (Figure 6(f)) exhibits a slight increase in bond length, from 1.48 Å to 1.49 Å, suggesting the presence of a small tensile strain induced by the surrounding cubic network. Its thickness also remains unchanged, maintaining a value of 3.4 Å before and after structural relaxation. These results indicate that, at the 80/20 proportion, the cubic phase predominantly governs the structural behavior of the heterostructure, while the remaining h-BN regions adapt locally to the lattice constraints imposed by the c-BN framework.

The magnetic behavior of the c-BN/h-BN heterostructures provides further support for the structural transformations discussed previously. Table 3 summarizes the magnetic properties observed for the c-BN/h-BN heterostructures after structural relaxation. For all initial configurations, an induced spin polarization was applied to the c-BN regions in order to investigate the magnetic response of the interfaces after structural relaxation. For the 20/80 and 40/60 heterostructures, the total magnetization becomes negligible after relaxation. This magnetic quenching is consistent with the structural reconstruction of the cubic regions into hexagonal-like configurations. As the sp^3 network collapses and the local atomic coordination approaches the sp^2-like arrangement characteristic of h-BN, the spin-polarized electronic states associated with the cubic phase are substantially suppressed.

In contrast, the heterostructures that preserve the coexistence of cubic and hexagonal regions (50/50, 60/40, and 80/20) retain distinct magnetic signatures after relaxation. The 50/50 heterostructure exhibits an absolute magnetization of 0.049 μB/atom and a total magnetization of -0.040 μB/atom. For the 60/40 proportion, the absolute magnetization increases to 0.060 μB/atom, while the total magnetization becomes approximately zero, suggesting an antiferromagnetic-like compensation between local magnetic moments. For the 80/20 heterostructure, the absolute and total magnetizations decrease to 0.032 μB/atom and -0.029 μB/atom, respectively. These results indicate that the magnetic behavior of the heterostructures is strongly correlated with the preservation of the sp^3-like cubic network and the thickness of the c-BN regions.

Overall, the emergence of magnetic signatures in the intermediate concentration regimes suggests that the coexistence of sp^2- and sp^3-like domains, together with the associated interfacial distortions, plays an important role in stabilizing localized spin polarization within the heterostructures.

4. Conclusion

In this work, we systematically investigated the structural stability and magnetic behavior of c-BN/h-BN heterostructures as a function of phase proportion using DFT calculations. Our results demonstrate that heterostructures containing low concentrations of c-BN (20/80 and 40/60) undergo pronounced structural reconstruction during relaxation, with the cubic regions evolving toward hexagonal-like configurations. Additional simulations performed for isolated c-BN slabs revealed the existence of a critical thickness required to preserve the sp^3-bonded cubic network, while the interaction with h-BN domains further facilitates the structural transformation of thin c-BN regions.

In contrast, heterostructures with higher c-BN concentrations (50/50, 60/40, and 80/20) preserve the coexistence of sp^2- and sp^3-like arrangements after relaxation. The Radial Distribution Function analysis confirmed the progressive stabilization of the cubic phase with increasing c-BN thickness, particularly for the 60/40 and 80/20 proportions, where only minor structural distortions and thickness variations were observed. The magnetic analysis revealed that the suppression of the sp^3 network leads to magnetic quenching in the low c-BN concentration heterostructures, while the preservation of cubic regions enables the emergence of localized magnetic ordering in the intermediate and high c-BN concentration regimes.

Overall, these findings demonstrate that the structural and magnetic properties of c-BN/h-BN heterostructures are strongly governed by the relative phase proportion and the thickness of the cubic domains. The present results provide important insights into the design of BN-based heterostructures with tunable structural and magnetic properties. Future experimental investigations will be valuable to validate the structural reconstruction mechanisms and critical c-BN thickness predicted by the present first-principles calculations.

5. Acknowledgments

We thank the Brazilian agency São Paulo Research Foundation (FAPESP) (grant 2023/08122-0) for financial support. Computational support from the Center for Scientific Computing (NCC/GridUNESP) of São Paulo State University (UNESP) is also acknowledged. This study was carried out with support from CNPq – National Council for Scientific and Technological Development – Brazil (process 304957/2023-2) and Coordenação de Aperfeiçoamento de Pessoal de Nível Superior - Brasil (CAPES) – Finance Code 001.

6. Data Availability

Data that support the findings of this study will be made available upon request to the corresponding author.

7. References

1. Lee CH, Kayastha VK, Wang J, Yap YK. Introduction to B–C–N Materials. In: Yap YK, editor. B-C-N Nanotubes and Related Nanostructures. New York: Springer; 2009. p. 1-22. https://doi.org/10.1007/978-1-4419-0086-9_1.
2. Haubner R, Wilhelm M, Weissenbacher R, Lux B. Boron nitrides: properties, synthesis and applications. In: Jansen M, editor. High Performance Non-Oxide Ceramics II. Berlin: Springer; 2002. p. 1-45. https://doi.org/10.1007/3-540-45623-6_1.
3. Mirkarimi PB, McCarty KF, Medlin DL. Review of advances in cubic boron nitride film synthesis. Mater Sci Eng Rep. 1997;21(2):47-100. https://doi.org/10.1016/S0927-796X(97)00009-0.
4. Wang J, Ma F, Sun M. Graphene, hexagonal boron nitride, and their heterostructures: properties and applications. RSC Adv. 2017;7(27):16801-22. https://doi.org/10.1039/c7ra00260b.
5. Zhang Y, Gao W, Li Y, Zhao D, Yin H. Hybrid fillers of hexagonal and cubic boron nitride in epoxy composites for thermal management applications. RSC Adv. 2019;9(13):7388-99. https://doi.org/10.1039/C9RA00282K. PMid:35519993.
6. Haque A, Narayan J. Conversion of h-BN into c-BN for tuning optoelectronic properties. Mater Adv. 2020;1(4):830-6. https://doi.org/10.1039/d0ma00008f.
7. Miwa RH, Schmidt TM, Guerini S. Theoretical investigation of the hBN(0001)/cBN(111) interface. Diam Relat Mater. 2008;17(11):1888-91.
8. Parra PA, Oliveira EF. Interfacial properties of composites based on h-BN and c-BN as a function of temperature: a molecular dynamics study. MRS Adv. 2025;10(12):1501-5. https://doi.org/10.1557/s43580-025-01157-3.
9. Xu M, He Z, Biswas A, Luo S, Li T, Chang C, et al. Modulation of dielectric properties of hexagonal/cubic boron nitride composites. Appl Phys Lett. 2024;124(19):192903. https://doi.org/10.1063/5.0210915.
10. Martin RM. Electronic structure: basic theory and practical methods. Cambridge: Cambridge University Press; 2004. https://doi.org/10.1017/CBO9780511805769.
11. Blöchl PE. Projector augmented-wave method. Phys Rev B Condens Matter. 1994;50(24):17953-79. https://doi.org/10.1103/PhysRevB.50.17953. PMid:9976227.
12. Grimme S, Antony J, Ehrlich S, Krieg H. A consistent and accurate ab initio parametrization of density functional dispersion correction (DFT-D) for the 94 elements H-Pu. J Chem Phys. 2010;132(15):154104. https://doi.org/10.1063/1.3382344. PMid:20423165.
13. Giannozzi P, Baroni S, Bonini N, Calandra M, Car R, Cavazzoni C, et al. QUANTUM ESPRESSO: a modular and open-source software project for quantum simulations of materials. J Phys Condens Matter. 2009;21(39):395502. https://doi.org/10.1088/0953-8984/21/39/395502. PMid:21832390.
14. Perdew JP, Burke K, Ernzerhof M. Generalized gradient approximation made simple. Phys Rev Lett. 1996;77(18):3865-8. https://doi.org/10.1103/PhysRevLett.77.3865. PMid:10062328.
15. Humphrey W, Dalke A, Schulten K. VMD: visual molecular dynamics. J Mol Graph. 1996;14(1):33-8, 27-8. https://doi.org/10.1016/0263-7855(96)00018-5. PMid:8744570.
16. Hanwell MD, Curtis DE, Lonie DC, Vandermeersch T, Zurek E, Hutchison GR. Avogadro: an advanced semantic chemical editor, visualization, and analysis platform. J Cheminform. 2012;4(1):17. https://doi.org/10.1186/1758-2946-4-17. PMid:22889332.
17. Jain A, Ong SP, Hautier G, Chen W, Richards WD, Dacek S, et al. Commentary: The Materials Project: A materials genome approach to accelerating materials innovation. APL Mater. 2013;1(1):011002. https://doi.org/10.1063/1.4812323.
18. Lynch RW, Drickamer HG. Effect of high pressure on the lattice parameters of diamond, graphite, and hexagonal boron nitride. J Chem Phys. 1966;44(1):181-4. https://doi.org/10.1063/1.1726442.
19. Pease RS. An X-ray study of boron nitride. Acta Crystallogr. 1952;5(3):356-61. https://doi.org/10.1107/S0365110X52001064.
20. Solozhenko VL. Refinement of the crystal structure of cubic boron nitride. Z Kristallogr Cryst Mater. 1988;184(1-4):275-7.
21. Yin J, Li J, Hang Y, Yu J, Tai G, Li X, et al. Boron nitride nanostructures: fabrication, functionalization and applications. Small. 2016;12(22):2942-68. https://doi.org/10.1002/smll.201600053. PMid:27073174.
22. Weng Q, Wang X, Wang X, Bando Y, Golberg D. Functionalized hexagonal boron nitride nanomaterials: emerging properties and applications. Chem Soc Rev. 2016;45(14):3989-4012. https://doi.org/10.1039/C5CS00869G. PMid:27173728.
23. Biswas A, Xu R, Christiansen-Salameh J, Jeong E, Alvarez GA, Li C, et al. Phase stability of hexagonal/cubic boron nitride nanocomposites. Nano Lett. 2023;23(15):6927-36. https://doi.org/10.1021/acs.nanolett.3c01537. PMid:37489836.
24. Park HS, Klein PA, Wagner GJ. A surface Cauchy–Born model for nanoscale materials. Int J Numer Methods Eng. 2006;68(10):1072-95. https://doi.org/10.1002/nme.1754.